Electronic Supplemental information

Organophosphonic acid and cerium functionalized antimonotungstate with electrochemical promise in biosensing bacterial dissimilatory sulfite reductase gene sequence

Zhigang Tang,[a] Wenshu Zhang,[a] Yalun Hu,[a] Xiaodan Jia,[a] Lina Meng,[a] Dan Wang,[a,b,*] Lijuan Chen,[a,*] and Junwei Zhao[a,*]

[a] *Henan Key Laboratory of Polyoxometalate Chemistry, College of Chemistry and Chemical Engineering, Henan University, Kaifeng 475004, China*

[b] *Henan Province Engineering Research Center of High Value Utilization to Natural Medical Resource in Yellow River Basin, School of Pharmacy, Henan University, Kaifeng 475004, China*

Fig. S1 (a) Structure of Eu^{3+}-embedded $[Eu_3(H_2O)_3(SbW_9O_{33})(W_5O_{18})_3]^{18-}$.[6] (b) Structure of TM-embedded $[M_2Sb_2W_{20}O_{70}(H_2O)_6]^{(14-2n)-}$ (M^{n+} = Co^{2+}, Ni^{2+}, Mn^{2+} or Fe^{3+}).[7] (c) Structure of $[(SbW_9O_{33})_4\{WO_2(H_2O)\}_2Ce_3(H_2O)_8(Sb_4O_4)]^{19-}$.[8] (d) Structure of $\{[Ln_4(H_2O)_6Sb_6O_4](SbW_{10}O_{37})_2(SbW_8O_{31})_2\}^{22-}$ (Ln = Dy^{3+}, Er^{3+}, Y^{3+}, Ho^{3+}).[9] (e) Structure of $[Sb^{III}_9Sb^{V}Ln_3O_{14}(H_2O)_3][(SbW_9O_{33})_3(PW_9O_{34})]^{23-}$(Ln = Ce^{3+}, Sm^{3+}, Eu^{3+}, Gd^{3+}, Tb^{3+}, Dy^{3+}).[10] (f) Structure of $[Sb_{15}Tb_7W_3O_{29}(OH)_3(DMF)(H_2O)_6(SbW_8O_{30})(SbW_9O_{33})_5]^{27-}$.[11] (g) Structure of $[Sb_7W_{36}O_{133}Ln_3M_2(CH_3COO)(H_2O)_8]^{17-}$ (Ln = La^{3+}–Gd^{3+}, M = Co^{2+}; Ln = Ce^{3+}, M = Ni^{2+}, Zn^{2+}).[12] (h) Structure of $[Ln_3Ni_9(OH)_9(SbW_9O_{33})_2(PW_9O_{34})_3(CH_3COO)_3]^{30-}$ (Ln = Dy^{3+}, Er^{3+}).[13] (i) Structure of $\{[Ln_3(CH_3COO)_3(HPO_3)(WO_4)][B\text{-}\alpha\text{-}SbW_9O_{33}]_3\}^{25-}$ (Ln = Eu^{3+}, Dy^{3+}, Ho^{3+}, Er^{3+}).[14] (j) Structure of $[Ln(H_2O)_8]_2[Fe_4(H_2O)_8(thr)_2][B\text{-}\beta\text{-}SbW_9O_{33}]_2$ (thr = L-threonine, Ln = Pr^{3+}, Nd^{3+}, Sm^{3+}, Eu^{3+}, Gd^{3+}, Dy^{3+}, Lu^{3+}).[15] (k) Structure of $[Ln_4(HP^{III})W_8(H_2O)_{12}(H_2ptca)_2O_{28}][SbW_9O_{33}]_2^{12-}$ (H_3ptca = 1,2,3-propanetricarboxylic acid, Ln = La^{3+}, Ce^{3+}, Pr^{3+}).[16] (l) Structure of $[Ln_4(H_2O)_{14}W_7O_{15}(H_2MA)_4][SbW_9O_{33}]_2[HP^{III}Sb^{III}W_{15}O_{54}]_2^{20-}$ (H_3MA = DL-malic acid, Ln = Pr^{3+}, Nd^{3+}).[17] (m) Structures of $[Ln_2(H_2O)_4\{WO_2(pic)\}_2(SbW_8O_{30})_2]^{10-}$ (Ln = La^{3+}, Pr^{3+}) and $[\{Ln(H_2O)\}\{Ln(pic)\}(Sb_3O_4)(SbW_8O_{31})(SbW_{10}O_{35})]_2^{24-}$ (Hpic = picolinic acid, Ln =Tb^{3+}, Dy^{3+}, Ho^{3+}).[18] (n) Structure of $[Ce(H_2O)_5(2,6\text{-}pdca)]_4[Fe_4(H_2O)_6(B\text{-}\beta\text{-}SbW_9O_{33})_2]^{2-}$ (2,6-H_2pdca = 2,6-pyridine-dicarboxylic acid).[19] Color codes: C, black; O, red; N, blue; Ln, plum; TM, yellow; Sb, orange; P, rose; W, turquiose balls; pale blue octahedra).

Fig. S2 Comparison of experimental PXRD and the corresponding simulated XRD patterns of **1**.

Fig. S3 The IR spectrum of **1**.

Fig. S4 The TG curve of **1**.

Fig. S5 The $\{Ce_3W_8(Hgps)_2\}$ core surrounded by four trivacant $\{SbW_9\}$ SBUs via twelve μ_2-O and ten μ_3-O atoms.

Fig. S6 The dihedral angle between the $Sb1W_9$–$Sb2W_9$–$Sb3W_9$ plane and $Sb2W_9$–$Sb3W_9$–$Sb4W_9$ plane in **1a**.

Fig. S7 (a) The dumbbell-shaped heterometallic $\{Ce_3W_8(Hgps)_2\}$ cluster in **1a** and the breakdown drawing of the $\{Ce_3W_8(Hgps)_2\}$ cluster. (b) Combination of $Hgps^{4-}$, $\{CeW_4\}$ and $Ce2^{3+}$.

Fig. S8 (a) Structure of **1a**. (b) Structure of **1a** after the removal of $Hgps^{4-}$ ligands.

Fig. S9 The monocapped square antiprismatic geometries of $Ce1^{3+}$ and $Ce3^{3+}$ ions and the bicapped trigonal prismatic configuration of the $Ce2^{3+}$ ion.

Fig. S10 (a–c) Packing architectures of **1** with a regular –ABAB– arrangement fashion in *bc*, *ac* or *ab* planes. (d–f)

Simplified quadrilateral of the **1a** polyanion viewed along *bc*, *ac* or *ab* planes. (g–i) Simplified packing representations of **1a** polyanions viewed along *bc*, *ac* or *ab* plane.

Fig. S11 (a) Hydrogen-bonding interactions between N atoms on $[H_2N(CH_3)_2]^+$ cations and surface O atoms of **1a** polyanions. (b) The distances between donor N9 atom and acceptor O atoms.

Fig. S12 (a) A mixture of **1,** GO and N_2H_4 after reaction for 2h at 60°C. (b) A mixture of GO and N_2H_4 after reaction for 2 h at 60°C.

Fig. S13 (a) Comparison of IR spectra of **1'**(red) obtained by re-precipitating **1** with using CsCl in water and **1** (blue). (b) Comparison of Raman spectra of **1** in water solution (black) and **1** in solid state (red). It's worth noting that the low signal intensity of **1** in water is most likely due to low solubility of **1**. (c) Comparison of UV-vis spectra of **1** in water under different storage times.

Fig. S14 The ESI-MS spectrum of **1** in aqueous solution and peak assignments with proposed formula and charge.

Fig. S15 The TEM-EDS elemental mapping images for the rGO-**1** with W, Sb, Ce, P, C and N elements.

Fig. S16 (a) IR spectra of GO, **1**, rGO-**1** and Au-rGO-**1**. (b) IR spectra of GO, **1** and rGO-**1**. (c) Raman spectra of GO, **1**, rGO-**1** and Au-rGO-**1**.

Fig. S17 The SEM-EDS elemental mapping images for the Au-rGO-**1** with W, Au, C, N, Sb, Ce and P elements.

Fig. S18 The Zeta potentials of GO, rGO-**1** and Au-rGO-**1**.

Fig. S19 (a) SWV curves of Au-rGO-**1**/GCEs stored for different times at room temperature in the $[Fe(CN)_6]^{3-/4-}$–K solution. (b) SWV curves of bare GCEs stored for different times at room temperature in the $[Fe(CN)_6]^{3-/4-}$–K solution.

Fig. S20 Schematic preparation of Au-rGO-**1**/GCE.

Fig. S21 CV curves of each modified electrode (bare GCE, Au-rGO-**1**/GCE, c-DNA/Au-rGO-**1**/GCE, MH-treated c-DNA/Au-rGO-**1**/GCE, dsDNA/Au-rGO-**1**/GCE and MB/dsDNA/Au-rGO-**1**/GCE) in the $[Fe(CN)_6]^{3-/4-}$–K solution.

Fig. S22 (a) SWV curves of MB/dsDNA/Au-rGO-**1**/GCEs constructed by using different concentrations of t-DNA (10^{-14} / 10^{-13} / 10^{-12} / 10^{-11} / 10^{-10} / 10^{-9} / 10^{-8} / 10^{-7} M). (b) SWV curves of the specificity of MB/dsDNA/Au-rGO-**1**/GCE EDB for different DNA sequences. (c) SWV curves of the anti-interference capability of MB/dsDNA/Au-rGO-**1**/GCE EDB different interference DNA sequences. (d) The time-dependent stability of MB/dsDNA/Au-rGO-**1**/GCE EDB for t-DNA detection after stored for 2, 3, 4, 5, 6 and 7 days. (e) The repeatability of five MB/dsDNA/Au-rGO-**1**/GCE EDBs. (f) SWV curves of MB/dsDNA/Au-rGO-**1**/GCEs constructed by using different concentrations of t-DNA (10^{-13} / 10^{-12} / 10^{-11} / 10^{-10} / 10^{-9} / 10^{-8} M) in human serum solution diluted 1000 times by using the Tris–HCl solution.

Table S1 Brief summary of experimental conditions of OLLFATs.

Table S2 Experimental explorations on the synthesis of 1.

Table S3 Crystallographic data and structure refinements for 1.

Table S4 Comparison of the sensitivity of different EDBs for DNA sequence detection.

Materials and physical measurements

The chemicals and reagents are commercially purchased and used without further purification. Elemental analyses (carbon, hydrogen and nitrogen) were measured on a Vario EL Cube CHNS analyzer. IR spectra were collected from a solid sample palletized with KBr on a Bruker VERTEX 70 IR spectrometer in the range 400–4000 cm^{-1}. Inductively coupled plasma atomic emission spectrometry (ICP–AES) was performed on a Perkin–Elmer Optima 2000 ICP–AES spectrometer. Powder X-ray diffraction (PXRD) pattern was obtained with Bruker D8 ADVANCE apparatus using Cu Kα radiation (λ = 1.54056 Å) at room temperature. The thermogravimetric (TG) analysis was carried out on a Mettler-Toledo TGA/SDTA 851^e thermal analyze instrument under N_2 atmosphere with temperature ranging from 25 °C to 1000 °C (heating rate: 10 °C min^{-1}). Scanning electron microscopy (SEM) images were recorded on a Carl Zeiss Gemini 500 field-emission scanning electron microscope equipped with energy-dispersive spectrometer (EDS). Transmission electron microscopy (TEM) images were obtained on a JEM–F200 electron microscope equipped with energy-dispersive spectrometer (EDS). Electrospray ionization mass spectrometry (ESI-MS) was performed on an AB SCIEX Triple TOF 4600 instrument. X-ray photoelectron spectroscopy (XPS) measurements were conducted using a ThermoFischer ESCALAB 250X instrument. The zeta potential was recorded on a Zetasizer NanoZS90 instrument. UV-vis spectra were recorded on a Mapada UV-6100 UV-vis spectrometer in the range of 190–600 nm in aqueous solution. Raman spectra were recorded on an Edinburgh RM5 Raman spectrometer with an excitation laser at 532 nm. Electrochemical tests were carried out by means of a CHI660E electrochemical workstation (Shanghai Chenhua Instruments, China) with a three-electrode system (modified GCE as working electrode, Ag/AgCl as reference electrode, and platinum column electrode as counter electrode). Cyclic voltammetry (CV) and Square wave voltammetry (SWV) were recorded in the 10.0 mM $K_3[Fe(CN)_6]$ / $K_4[Fe(CN)_6]^{4-}$(1:1) solution containing and 100 mM KCl (marked as $[Fe(CN)_6]^{3-/4-}$–K) and the Tris–HCl solution (0.10 M tris(hydroxymethyl)aminomethane hydrochloride buffer solution containing 20.0 mM NaCl, pH = 8.00).

X-ray crystallography

Diffraction intensity data of a high-quality single-crystal of **1** were collected on a Bruker D8 Venture Photon II diffractometer with Mo Kα radiation (λ = 0.71073 Å) at 150 K. Direct methods were used to solve the structure of **1** and locate the heavy atoms. The structure was refined on F^2 by full-matrix least-squares method using the SHELXTL 97 program.[1,2] The remaining atoms were found from successive full-matrix least-squares refinements on F2 and Fourier syntheses. All hydrogen atoms attached to carbon and nitrogen atoms were geometrically placed and refined isotropically as a riding model using the default SHELXTL parameters. No hydrogen atoms associated with water molecules were located from the difference Fourier map. All non-hydrogen atoms except for some Na, C, N, O and some water atoms were refined anisotropically. In the refinement of **1**, sixty-two lattice water molecules and seven $[H_2N(CH_3)_2]^+$ cations in the molecular unit were found from the Fourier maps. However, there are still solvent accessible voids in the check cif report of crystal structure of **1**, indicating that some lattice water molecules or cations should exist in the structure that can't be found from the weak residual electron peaks. Therefore, on the basis of charge balance, elemental analysis and TG analysis, two $[H_2N(CH_3)_2]^+$ cations six protons and four lattice water molecules were directly added to the molecular formula of **1**. This phenomenon that organoanime cations and lattice are directly added to the molecular formula according to the results of elemental

analysis and TG analysis is very common in POM compounds.[3–5] The crystallographic data and structure refinement parameters for **1** are demonstrated in Table S3. The cif file of **1** reported in this paper has been deposited at the Cambridge Crystallographic Data Centre with CCDC 2236459, which can be obtained free of charge from the Cambridge Crystallographic Data Centre via www.ccdc. cam.ac.uk/data_request/cif.

Preparation of the $SbCl_3$ solution

The solid $SbCl_3$ (13.700 g, 0.060 mol) was completely dissolved in hydrochloric acid (HCl) solution (6.0 M, 60.00 mL). The concentration of Sb^{3+} ions is 1.000 mM.

Synthesis of the rGO-1 composite material

Graphene oxide (GO, 15.000 mg) was dispersed into water (5.00 mL), forming the GO colloidal dispersion (3.00 mg mL^{-1}) and sonicated for 4 h. Then, **1** (70.000 mg) in 1.00 mL water and hydrazine hydrate (0.20 mL, 80 wt%) were added into the above dispersion. The resultant mixture was kept at 60 °C for 2 h and cooled to room temperature. Then, the rGO-**1** composite material was formed and washed three times by using 5.00 mL N,N-dimethylformamide (DMF) per time and lyophilized for one day.

Synthesis of the Au-rGO-1 composite material

Graphene oxide (GO, 15.000 mg) was dispersed into water (5.00 mL), forming the GO colloidal dispersion (3.00 mg mL^{-1}) and sonicated for 4 h. Then, **1** (70.000 mg) in 1.00 mL water, $HAuCl_4{\cdot}3H_2O$ solution (10.00 mg mL^{-1}, 0.20 mL) and hydrazine hydrate (0.20 mL, 80 wt%) were added into the above dispersion. The resultant mixture was kept at 60 °C for 2 h and cooled to room temperature. Then, the Au-rGO-**1** composite material was formed and washed three times by using 5.00 mL DMF per time and lyophilized for one day.

Synthesis of the p-GO composite material

Graphene oxide (GO, 15.000 mg) was dispersed into water (5.00 mL), forming the GO colloidal dispersion (3.00 mg mL^{-1}) and sonicated for 4 h. Then, hydrazine hydrate (0.20 mL, 80 wt%) was added into the above dispersion. The resultant mixture was kept at 60 °C for 2 h and cooled to room temperature. Then, the p-GO composite material was formed and washed three times by using 5.00 mL DMF per time and lyophilized for one day.

Preparations of oligonucleotides and buffer solution used for electrochemical measurement

All oligonucleotides in this work were purchased from Shanghai Sangon Biological Engineering Technological Co. Ltd. (China) with the following sequences:

Complementary DNA (c-DNA): 5'−HS-ACGTAGTTGTGGTACGGGGCGCG−3'.

Target DNA (t-DNA): 5'−CGCGCCCCGTACCACAACTACGT−3'.

Single-base mismatch DNA (1-MT): 5'−CGCGCCCCGTAGCACAACTACGT−3'.

Three-base mismatch DNA (3-MT): 5'−CGCGTCCCGTAGCACAACGACGT−3'.

Non-complementary DNA (NC): 5'−AGTACATATCGAGTACCTTCATG−3'.

Tris-ethylenediaminetetraacetic acid (TE) buffer (pH = 7.40) containing 10.0 mM tris(hydroxymethyl) aminomethane and 1.0 mM ethylenediaminetetraacetic acid, was purchased from Innochem (Beijing, China). All of DNAs were dissolved with TE buffer (pH = 7.40).

Construction process of the MB/dsDNA/Au-rGO-1/GCE EDB is described as follows:

Preparation of Au-rGO-1/GCE

GCE was artificially polished to a mirror-like surface using 0.05 μm alumina power on a clean gauze and cleaned with ethanol and water. Then, 5.0 μL suspension of Au-rGO-**1** (3.00 mg was dispersed in 1.00 mL DMF under sonication for 1.0 h) was dropped onto the GCE surface and quiescently dried at 37 ^{o}C. The formed electrode is donated as Au-rGO-**1**/GCE.

Preparation of c-DNA/Au-rGO-1/GCE

Then the 5'-thiolated single-stranded DNA solution (8.0 μL) was chosen as the complementary DNA (c-DNA, 1 × 10^{-6} M) and immobilized on the Au-rGO-**1**/GCE surface and then permitted to stand at room temperature for 2.0 h to adhere to c-DNA strands on the surface of Au-rGO-**1**/GCE via strong Au–S bands. The formed electrode is donated as c-DNA/Au-rGO-**1**/GCE.

Preparation of MH-treated c-DNA/Au-rGO-1/GCE

8.0 μL of 6-mercapto-1-hexanol (MH, 1.0 mM) was covered on the surface of c-DNA/Au-rGO-**1**/GCE, which was kept at room temperature for 30 min for blocking nonspecific binding-sites of Au nanoparticles and also helping the c-DNA stay in proper orientation for adequate recognition ability. The formed electrode is donated as MH-treated c-DNA/Au-rGO-**1**/GCE.

Preparation of dsDNA/Au-rGO-1/GCE

8.0 μL target-DNA (t-DNA) testing solutions containing various concentrations of t-DNA (c = 10^{-14} / 10^{-13} / 10^{-12} / 10^{-11} / 10^{-10} / 10^{-9} / 10^{-8} / 10^{-7} M) were respectively dropped onto the surface of MH-treated c-DNA/Au-rGO-**1**/GCEs for 60 min to construct dsDNA/Au-rGO-**1**/GCEs.

Preparation of MB/dsDNA/Au-rGO-1/GCE

The MB solution (20 μM, 20.0 μL) was dropped on the surface of dsDNA/Au-rGO-**1**/GCE, which was kept for 20 min to sufficiently adsorb MB in order to enhance signal readout. The formed electrode is donated as MB/dsDNA/Au-rGO-**1**/GCE.

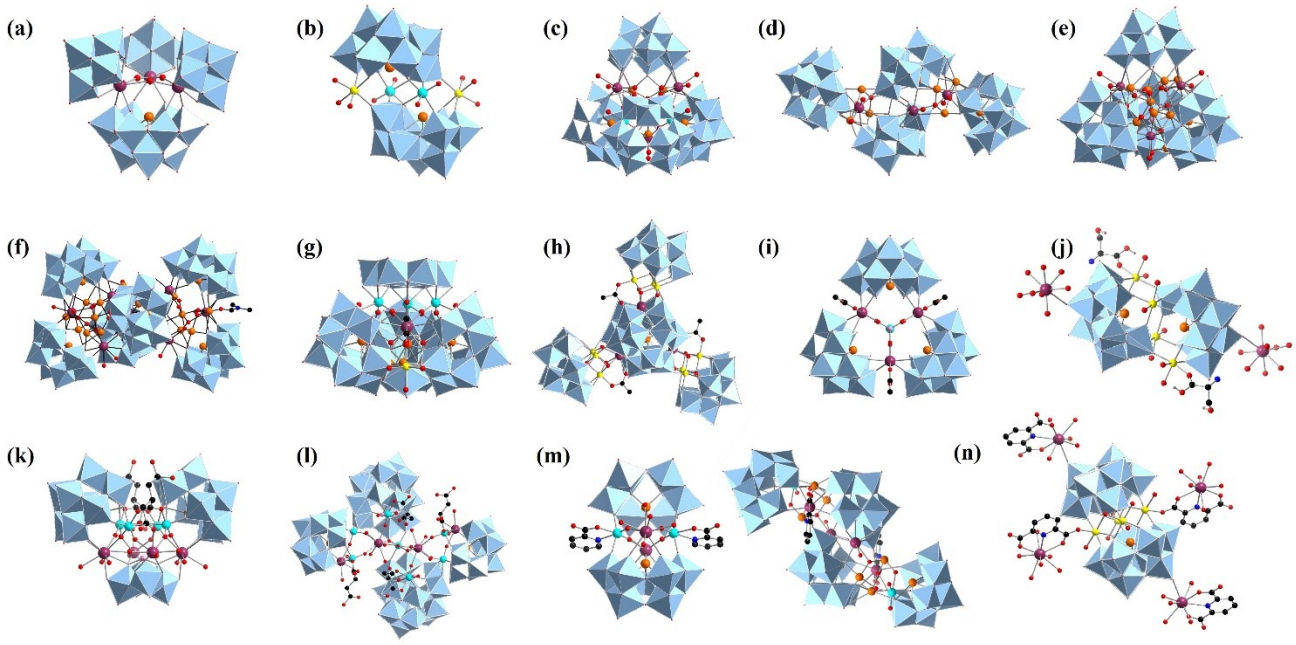

Fig. S1 (a) Structure of Eu^{3+}-embedded $[Eu_3(H_2O)_3(SbW_9O_{33})(W_5O_{18})_3]^{18-}$.[6] (b) Structure of TM-embedded $[M_2Sb_2W_{20}O_{70}(H_2O)_6]^{(14-2n)-}$ (M^{n+} = Co^{2+}, Ni^{2+}, Mn^{2+} or Fe^{3+}).[7] (c) Structure of $[(SbW_9O_{33})_4\{WO_2(H_2O)\}_2Ce_3(H_2O)_8(Sb_4O_4)]^{19-}$.[8] (d) Structure of $\{[Ln_4(H_2O)_6Sb_6O_4](SbW_{10}O_{37})_2(SbW_8O_{31})_2\}^{22-}$ (Ln = Dy^{3+}, Er^{3+}, Y^{3+}, Ho^{3+}).[9] (e) Structure of $[Sb^{III}_9Sb^{V}Ln_3O_{14}(H_2O)_3][(SbW_9O_{33})_3(PW_9O_{34})]^{23-}$(Ln = Ce^{3+}, Sm^{3+}, Eu^{3+}, Gd^{3+}, Tb^{3+}, Dy^{3+}).[10] (f) Structure of $[Sb_{15}Tb_7W_3O_{29}(OH)_3(DMF)(H_2O)_6(SbW_8O_{30})(SbW_9O_{33})_5]^{27-}$.[11] (g) Structure of $[Sb_7W_{36}O_{133}Ln_3M_2(CH_3COO)(H_2O)_8]^{17-}$ (Ln = La^{3+}–Gd^{3+}, M = Co^{2+}; Ln = Ce^{3+}, M = Ni^{2+}, Zn^{2+}).[12] (h) Structure of $[Ln_3Ni_9(OH)_9(SbW_9O_{33})_2(PW_9O_{34})_3(CH_3COO)_3]^{30-}$ (Ln = Dy^{3+}, Er^{3+}).[13] (i) Structure of $\{[Ln_3(CH_3COO)_3(HPO_3)(WO_4)][B\text{-}\alpha\text{-}SbW_9O_{33}]_3\}^{25-}$ (Ln = Eu^{3+}, Dy^{3+}, Ho^{3+}, Er^{3+}).[14] (j) Structure of $[Ln(H_2O)_8]_2[Fe_4(H_2O)_8(thr)_2][B\text{-}\beta\text{-}SbW_9O_{33}]_2$ (thr = L-threonine, Ln = Pr^{3+}, Nd^{3+}, Sm^{3+}, Eu^{3+}, Gd^{3+}, Dy^{3+}, Lu^{3+}).[15] (k) Structure of $[Ln_4(HP^{III})W_8(H_2O)_{12}(H_2ptca)_2O_{28}][SbW_9O_{33}]_2^{12-}$ (H_3ptca = 1,2,3-propanetricarboxylic acid, Ln = La^{3+}, Ce^{3+}, Pr^{3+}).[16] (l) Structure of $[Ln_4(H_2O)_{14}W_7O_{15}(H_2MA)_4][SbW_9O_{33}]_2[HP^{III}Sb^{III}W_{15}O_{54}]_2^{20-}$ (H_3MA = DL-malic acid, Ln = Pr^{3+}, Nd^{3+}).[17] (m) Structures of $[Ln_2(H_2O)_4\{WO_2(pic)\}_2(SbW_8O_{30})_2]^{10-}$ (Ln = La^{3+}, Pr^{3+}) and $[\{Ln(H_2O)\}\{Ln(pic)\}(Sb_3O_4)(SbW_8O_{31})(SbW_{10}O_{35})]_2^{24-}$ (Hpic = picolinic acid, Ln =Tb^{3+}, Dy^{3+}, Ho^{3+}).[18] (n) Structure of $[Ce(H_2O)_5(2,6\text{-}pdca)]_4[Fe_4(H_2O)_6(B\text{-}\beta\text{-}SbW_9O_{33})_2]^{2-}$ ($2,6\text{-}H_2pdca$ = 2,6-pyridine-dicarboxylic acid).[19] Color codes: C, black; O, red; N, blue; Ln, plum; TM, yellow; Sb, orange; P, rose; W, turquiose balls; pale blue octahedra).

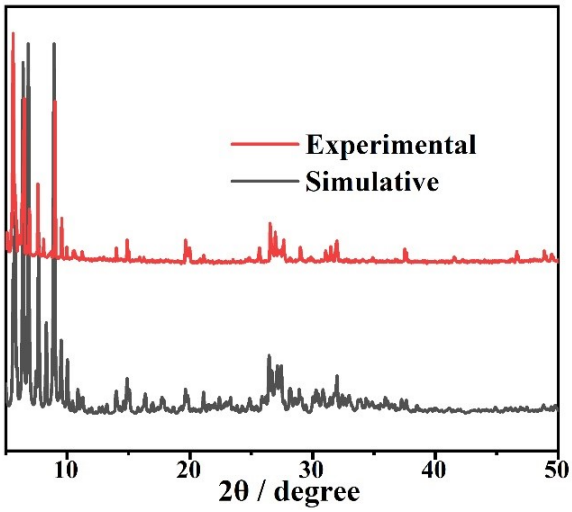

Fig. S2 Comparison of experimental PXRD and the corresponding simulated XRD patterns of **1**.

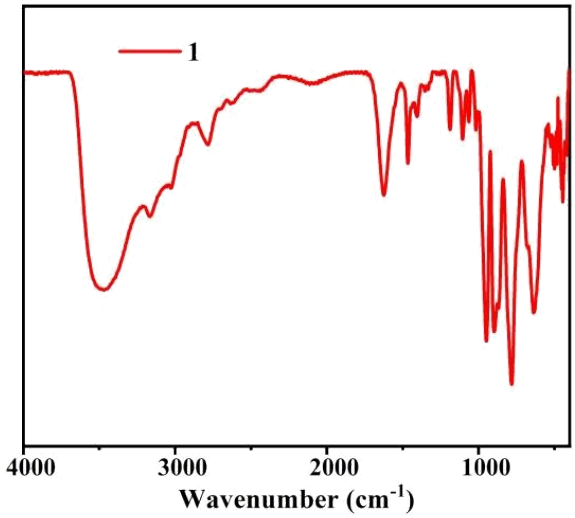

Fig. S3 The IR spectrum of **1**.

The IR spectrum of crystalline **1** has been measured using the solid sample palletized with KBr (Fig. S3), it can be found that a strong and wide absorption band at 3468–3395 cm^{-1} is assigned as the stretching vibration from O–H groups of lattice and coordination water molecules. And the weak absorption band appearing at 3174–3166 cm^{-1} and the weak absorption band at 2802–2782 cm^{-1} respectively correspond to the stretching vibrations of N–H and C–H bonds from $[H_2N(CH_3)_2]^+$ cations.[20,21] In the middle wavenumber region, one sharp absorption band at 1634–1626 cm^{-1} is derived from the bending vibration from O–H bands of lattice and coordination water molecules, the weak band at 1466–1463 cm^{-1} stems from the bending vibration of the C–H bands of $[H_2N(CH_3)_2]^+$ cations and the weak peaks at 1106 cm^{-1} and 1063 cm^{-1} are ascribed to the stretching vibrations of the P–O bands of OPA ligands.[14] In the low wavenumber region, the characteristic vibration peaks of the polyanion skeleton of **1** are observed at 950 cm^{-1} (ν_{W-Ot}), 869 cm^{-1} (ν_{W-Ob}) and 782 cm^{-1} (ν_{W-Oc}) and 683 cm^{-1} (ν_{Sb-O}).[16]

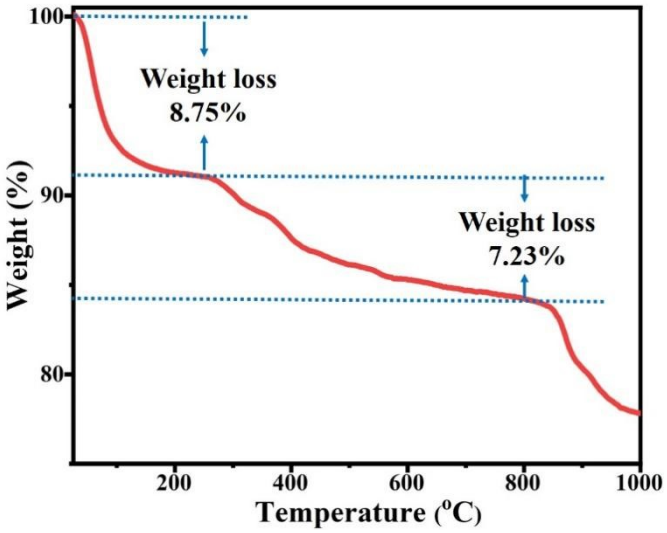

Fig. S4 The TG curve of **1**.

For the sake of exploring the thermal stability of **1**, the TG measurement was carried out from 25 to 1000 °C under a N_2 atmosphere at a heating rate of 10 °C min^{-1}. The TG curve suggests that **1** undergoes three steps weight loss (Fig. S4). From 25 to 250 °C, the first weight loss of 8.75% (calcd. 8.83%) is attributed to the liberation of sixty-six lattice water molecules and two coordination water molecules. With temperature increasing from 250 to 800 °C, the second weight loss of 7.23% (calcd. 7.41%) is assigned to the removal of nine dimethylamine groups, the dehydration of six protons and two Hgps ligands. Subsequently, the skeleton of **1** begins to collapse as the temperature further increases (> 800 °C) and some of WO_3 begin to sublimate.

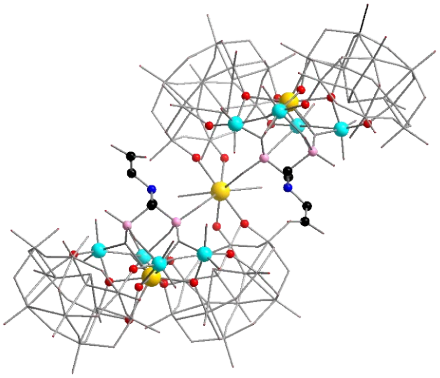

Fig. S5 The $\{Ce_3W_8(Hgps)_2\}$ core surrounded by four trivacant $\{SbW_9\}$ SBUs via twelve μ_2-O and ten μ_3-O atoms.

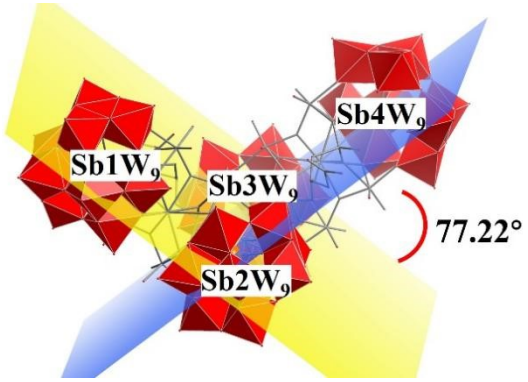

Fig. S6 The dihedral angle between the $Sb1W_9$–$Sb2W_9$–$Sb3W_9$ plane and $Sb2W_9$–$Sb3W_9$–$Sb4W_9$ plane in **1a**.

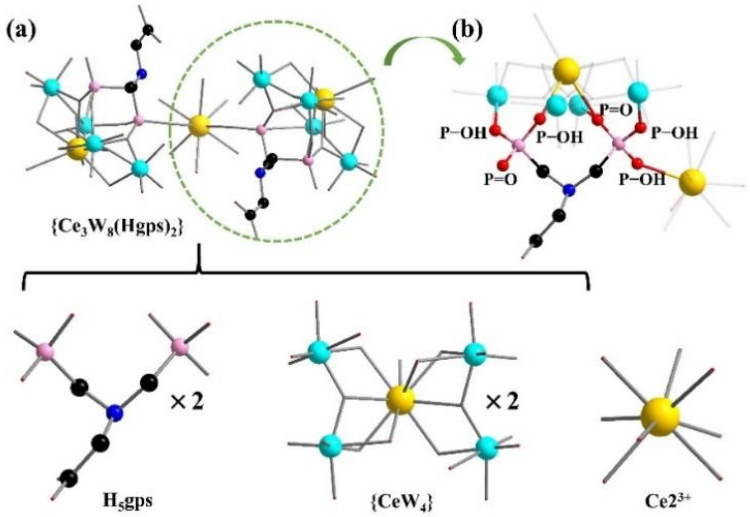

Fig. S7 (a) The dumbbell-shaped heterometallic $\{Ce_3W_8(Hgps)_2\}$ cluster in **1a** and the breakdown drawing of the $\{Ce_3W_8(Hgps)_2\}$ cluster. (b) Combination of $Hgps^{4-}$, $\{CeW_4\}$ and $Ce2^{3+}$.

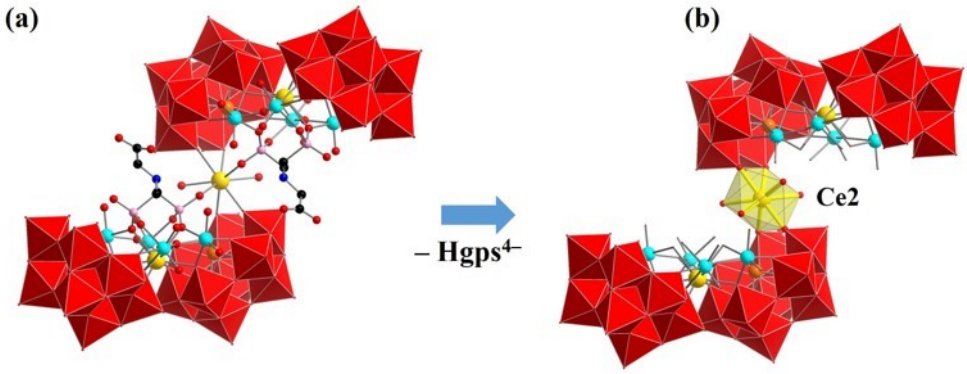

Fig. S8 (a) Structure of **1a**. (b) Structure of **1a** after the removal of $Hgps^{4-}$ ligands.

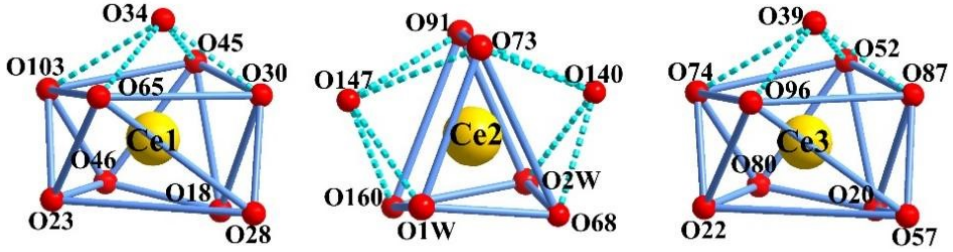

Fig. S9 The monocapped square antiprismatic geometries of $Ce1^{3+}$ and $Ce3^{3+}$ ions and the bicapped trigonal prismatic configuration of the $Ce2^{3+}$ ion.

Three crystallographically independent Ce^{3+} ions in **1a** adopt two different coordination geometries. $Ce1^{3+}$ and $Ce3^{3+}$ ions reside in the nine-coordinate distorted monocapped square antiprismatic geometry, in which the coordination sphere of the $Ce1^{3+}$ ion is established by five O atoms (O18, O28, O30, O23, O65) from the $\{SbW_9\}$ SBU, two O atoms (O45, O103) from the $Hgps^{4-}$ ligand and two O atoms (O34, O46) from the $\{W_4\}$ unit. The coordination geometry of the $Ce3^{3+}$ ion is formed by five O atoms (O20, O22, O57, O87, O96) from the $\{SbW_9\}$ SBU, two O atoms (O52, O74) from the $Hgps^{4-}$ ligand and two O atoms (O39, O80) from the $\{W_4\}$ unit. The $Ce2^{3+}$ ion displays an eight-coordinate twisted bicapped trigonal prismatic geometry that is established by two O atoms (O73 and O91) of two $Hgps^{4-}$ ligands and four O atoms (O68, O140, O147 and O160) from the $\{SbW_9\}$ SBU and two water ligands (O1W and O2W).

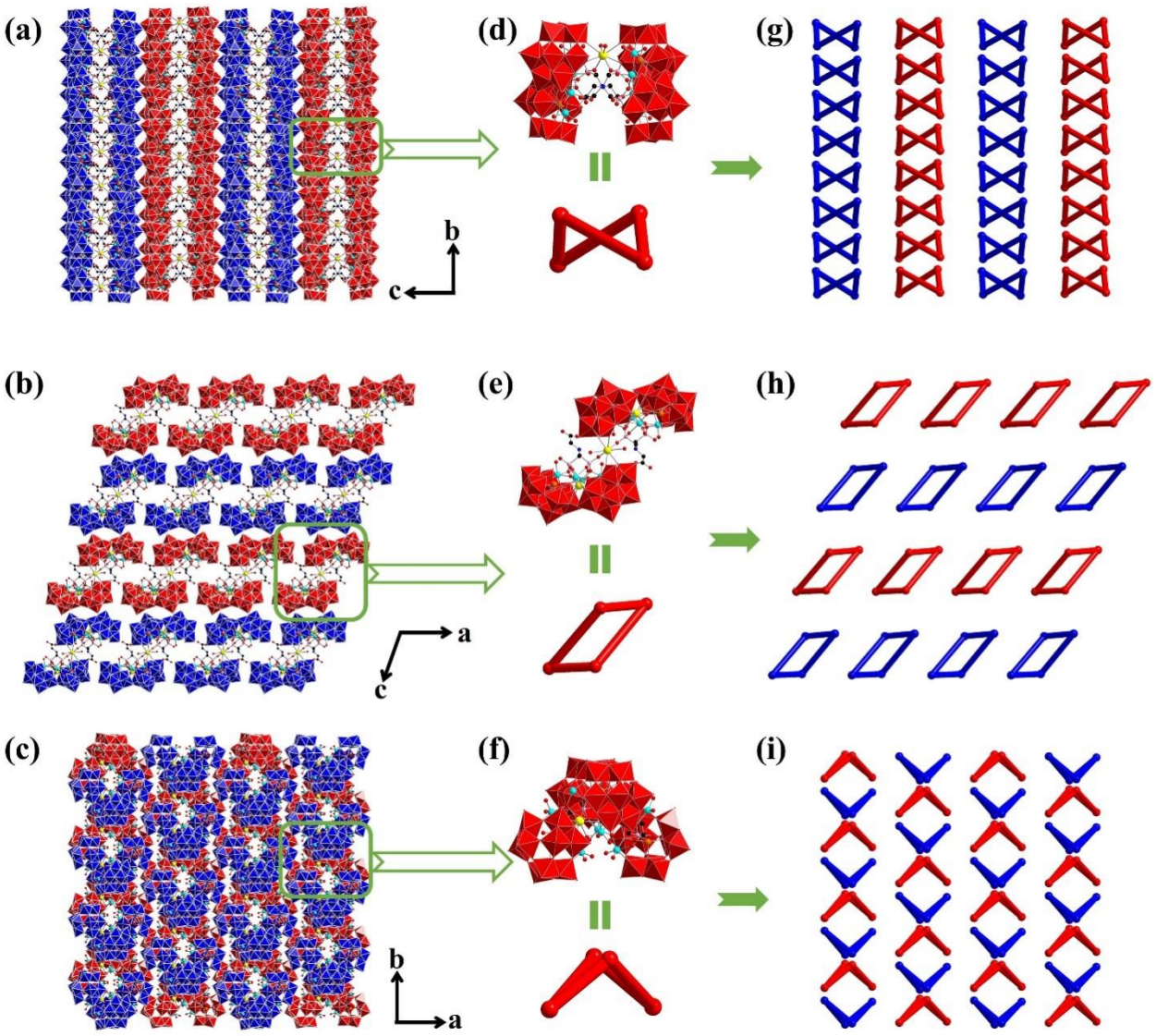

Fig. S10 (a–c) Packing architectures of **1** with a regular –ABAB– arrangement fashion in *bc*, *ac* or *ab* planes. (d–f) Simplified quadrilateral of the **1a** polyanion viewed along *bc*, *ac* or *ab* planes. (g–i) Simplified packing representations of **1a** polyanions viewed along *bc*, *ac* or *ab* plane.

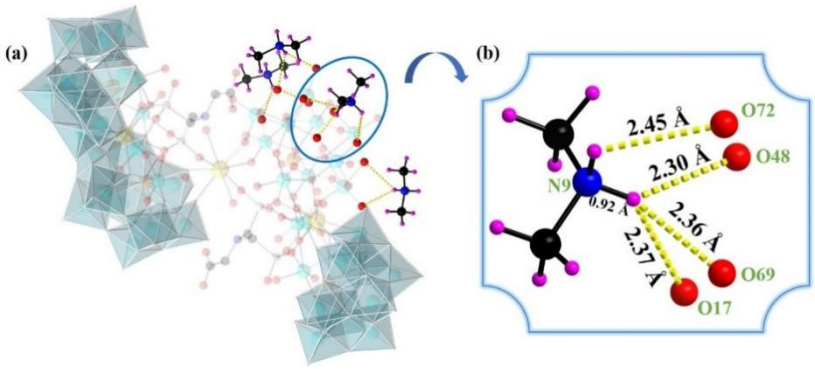

Fig. S11 (a) Hydrogen-bonding interactions between N atoms on $[H_2N(CH_3)_2]^+$ cations and surface O atoms of **1a** polyanions. (b) The distances between donor N9 atom and acceptor O atoms.

The **1a** polyanions regularly stack in a –ABAB– mode in *ab*, *ac* or *bc* plane (Fig.S10a–c). If each **1a** polyanion is simplified as a quadrilateral (Fig. S10d–f), the spatial packing for **1a** polyanions could be easier to understand (Fig. S10g–i). Along the *a* and *b* axes, neighboring **1a** polyanions are arranged in parallel, but along the *c* axis, adjacent

1a polyanions are arranged in the opposite patterns. Space utilization is able to effectively increase by the opposite arrangement of **1a** polyanions and access the most closely packing fashion. Besides, the space of **1a** polyanions was full of $[H_2N(CH_3)_2]^+$ cations and crystal water molecules. The hydrogen-bonding interactions between nitrogen atoms on $[H_2N(CH_3)_2]^+$ cations and oxygen atoms on the surface of **1a** polyanions and water molecules exist in the orderly stacking (Fig. S11a). It can be clearly observed that N−H···O distances are in 2.85(4)−3.30(2) Å (Fig. S11b).

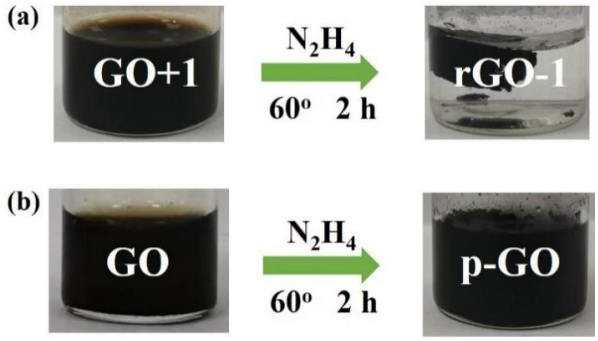

Fig. S12 (a) A mixture of **1,** GO and N_2H_4 after reaction for 2h at 60°C. (b) A mixture of GO and N_2H_4 after reaction for 2 h at 60°C.

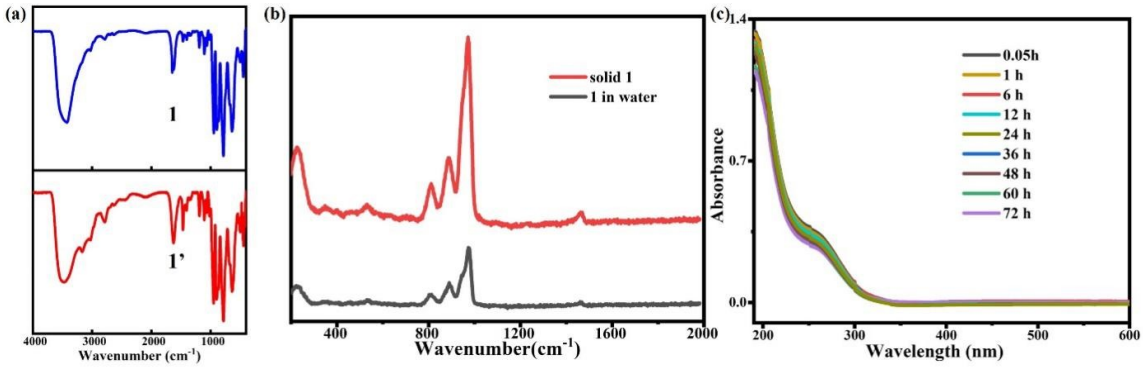

Fig. S13 (a) Comparison of IR spectra of **1'**(red) obtained by re-precipitating **1** with using CsCl in water and **1** (blue). (b) Comparison of Raman spectra of **1** in water solution (black) and **1** in solid state (red). It's worth noting that the low signal intensity of **1** in water is most likely due to the low solubility of **1**. (c) Comparison of UV-vis spectra of **1** in water under different storage times.

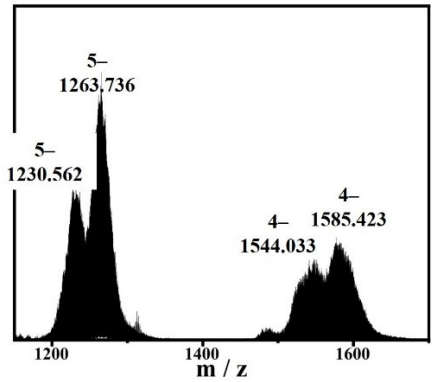

z	m/z (exp)	m/z (calc)	Assignment
5–	1230.562	1230.453	$\{Na_3H_4[Ce_2(H_2O)_2W_4(Hgps)O_{10}][SbW_9O_{33}]_2\}^{5-}$
5–	1263.736	1263.568	$\{Na_2[H_2N(CH_3)_2]_8[CeW_4(Hgps)O_{10}][SbW_9O_{33}]_2\}^{5-}$
4–	1544.033	1543.814	$\{Na_4H_4[Ce_2(H_2O)_2W_4(Hgps)O_{10}][SbW_9O_{33}]_2\}^{4-}$
4–	1585.423	1585.208	$\{Na_3[H_2N(CH_3)_2]_8[CeW_4(Hgps)O_{10}][SbW_9O_{33}]_2\}^{4-}$

Fig. S14 The ESI-MS spectrum of **1** in aqueous solution and peak assignments with proposed formula and charge.

As shown in the electrospray ionization mass spectrometry (ESI-MS) of **1** in aqueous solution (Fig. S14), the *m/z* = 1230.562 (5–) peak is assigned to $\{Na_3H_4[Ce_2(H_2O)_2W_4(Hgps)O_{10}][SbW_9O_{33}]_2\}^{5-}$, the *m/z* = 1263.736 (5–) peak is assigned to $\{Na_2[H_2N(CH_3)_2]_8[CeW_4(Hgps)O_{10}][SbW_9O_{33}]_2\}^{5-}$, the *m/z* = 1544.033 (4–) peak is assigned to $\{Na_4H_4[Ce_2(H_2O)_2W_4(Hgps)O_{10}][SbW_9O_{33}]_2\}^{4-}$, the *m/z* = 1585.423 (4–) peak is assigned to $\{Na_3[H_2N(CH_3)_2]_8[CeW_4(Hgps)O_{10}][SbW_9O_{33}]_2\}^{4-}$. The experimental *m/z* values (1230.562, 1263.736, 1544.033, 1585.423) are in good agreement calculated *m/z* values (1230.453, 1263.568, 1543.814, 1585.208) of **1**, which prove the good stability of the polyoxoanion of **1** in aqueous solution.

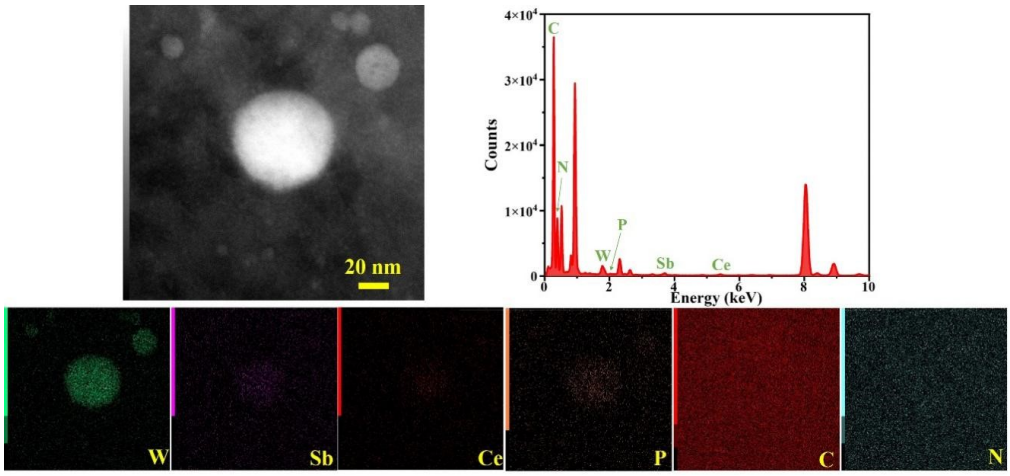

Fig. S15 The TEM-EDS elemental mapping images for the rGO-**1** with W, Sb, Ce, P, C and N elements.

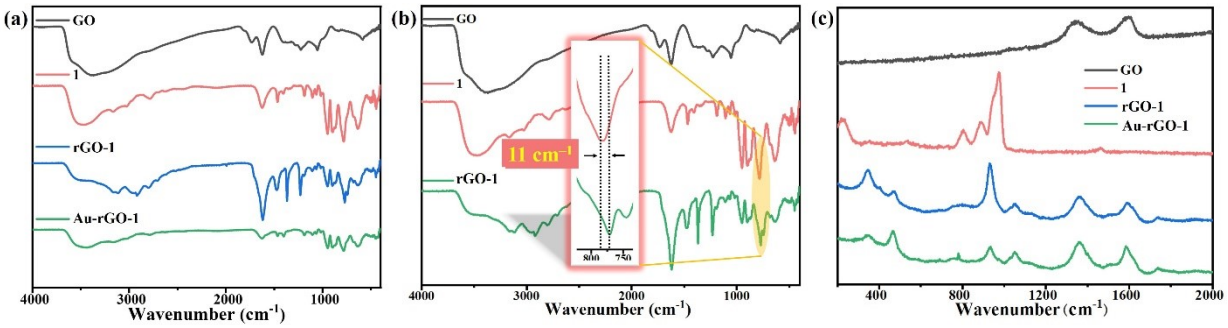

Fig. S16 (a) IR spectra of GO, **1**, rGO-**1** and Au-rGO-**1**. (b) IR spectra of GO, **1** and rGO-**1**. (c) Raman spectra of GO, **1**, rGO-**1** and Au-rGO-**1**.

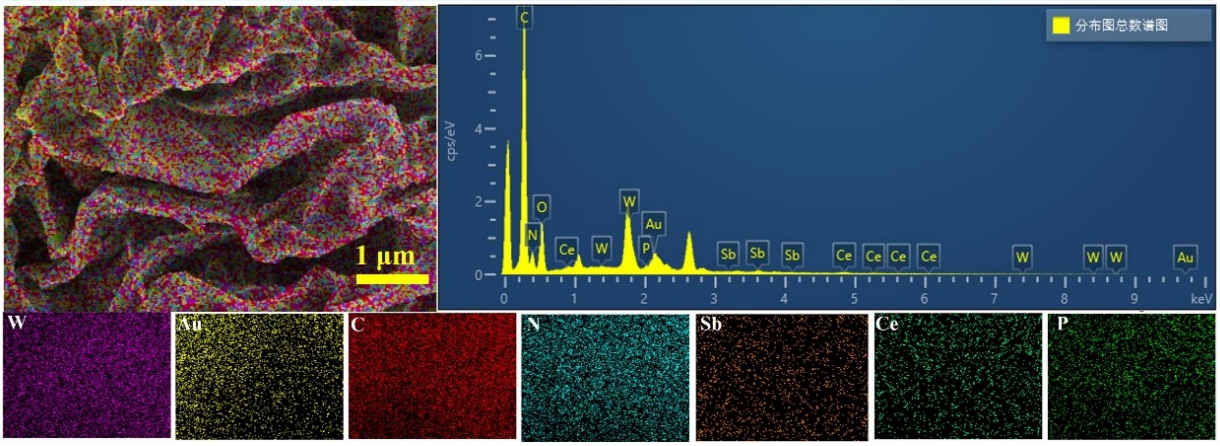

Fig. S17 The SEM-EDS elemental mapping images for the Au-rGO-**1** with W, Au, C, N, Sb, Ce and P elements.

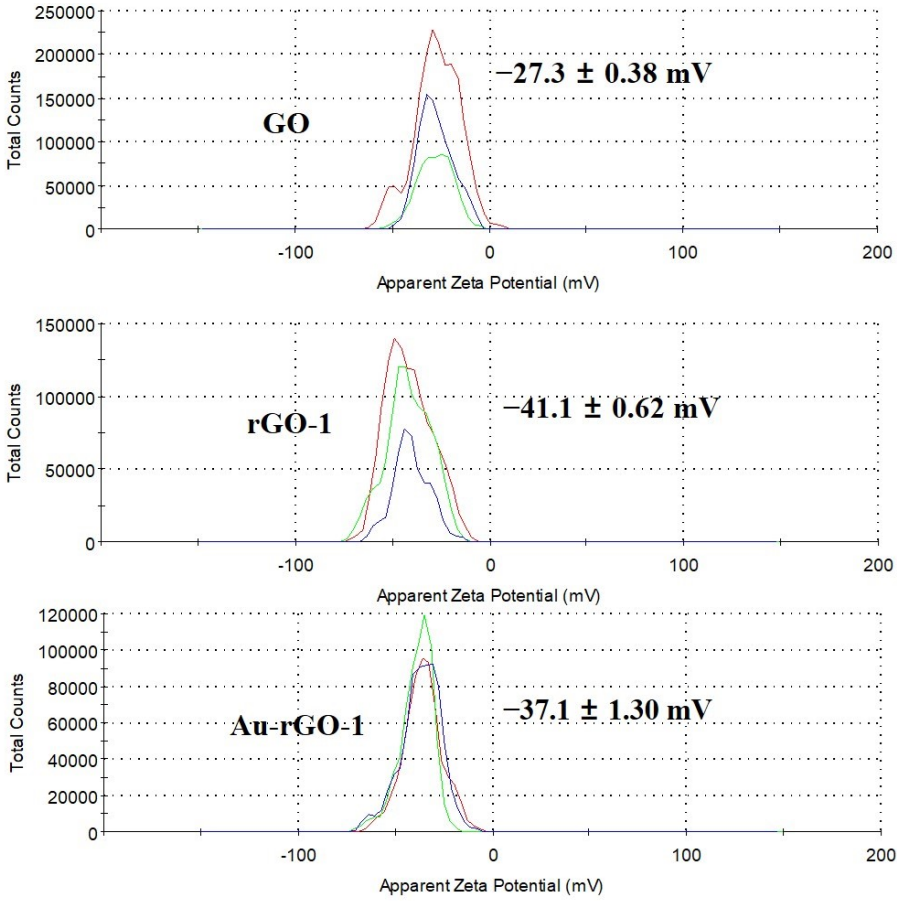

Fig. S18 The Zeta potentials of GO, rGO-**1** and Au-rGO-**1**.

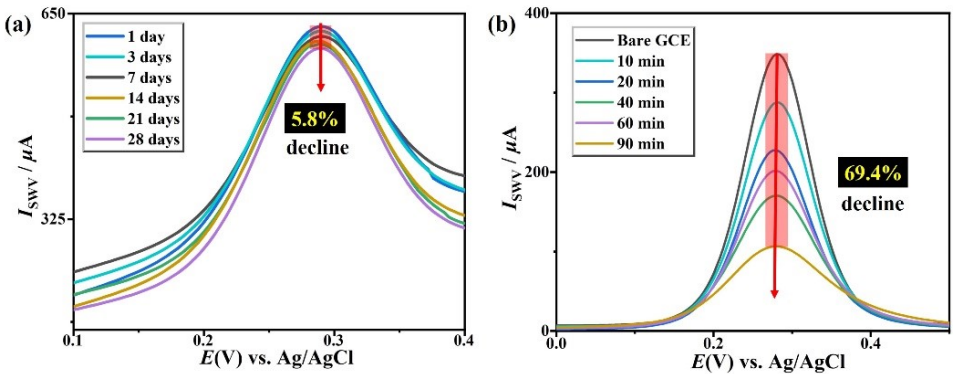

Fig. S19 (a) SWV curves of Au-rGO-**1**/GCEs stored for different times at room temperature in the $[Fe(CN)_6]^{3-/4-}$–K solution. (b) SWV curves of bare GCEs stored for different times at room temperature in the $[Fe(CN)_6]^{3-/4-}$–K solution.

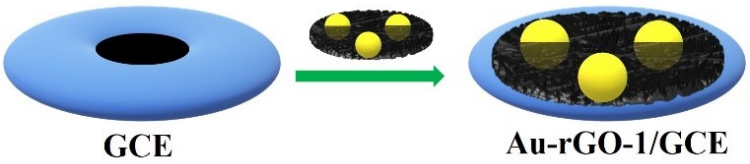

Fig. S20 Schematic preparation of Au-rGO-**1**/GCE.

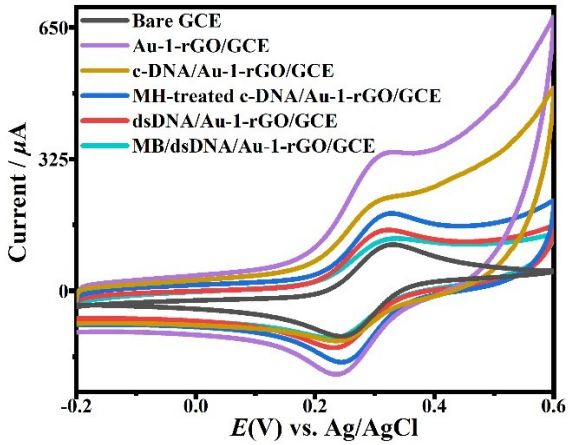

Fig. S21 CV curves of each modified electrode (bare GCE, Au-rGO-**1**/GCE, c-DNA/Au-rGO-**1**/GCE, MH-treated c-DNA/Au-rGO-**1**/GCE, dsDNA/Au-rGO-**1**/GCE and MB/dsDNA/Au-rGO-**1**/GCE) in the $[Fe(CN)_6]^{3-/4-}$–K solution.

In order to explain the change of electrode surface and provide persuasive evidence of the construction of the MB/dsDNA/Au-rGO-**1**/GCE EDB. The current signal of each modified electrode (bare GCE, Au-rGO-**1**/GCE, c-DNA/Au-rGO-**1**/GCE, MH-treated c-DNA/Au-rGO-**1**/GCE, dsDNA/Au-rGO-**1**/GCE and MB/dsDNA/Au-rGO-**1**/GCE) was monitored by CV method in the $[Fe(CN)_6]^{3-/4-}$–K solution. As shown in Fig. S21, the peak current observably increases compared with bare GCE when Au-rGO-**1** is assembled on the surface of electrode, indicating that Au-rGO-**1**/GCE performs excellent electron transfer property, which is beneficial for improving the sensitivity of the biosensor. After attachment of c-DNA on the Au-rGO-**1**/GCE surface, the peak current clearly decreases, resulting from the reduction of electrical conductivity due to the electrostatic repulsion between c-DNA with $[Fe(CN)_6]^{3/4-}$. Moreover, with the introduction of MH, the superfluous Au NPs are blocked accompanying with the decrease of active area, leading to decline of the peak current. After t-DNA was immobilized on the MH-treated c-DNA/Au-rGO-**1**/GCE surface by hybridizing with c-DNA forming double-stranded DNA (dsDNA) on the electrode surface (dsDNA/Au-rGO-**1**/GCE), the dsDNA further increases the negative charge, resulting in the further decrease of the peak current. Finally, the introduction of MB brings greater steric hindrance, which makes the peak current drop again. All of the above results successfully demonstrate the electrode surface change and provide persuasive evidence of the construction of MB/dsDNA/Au-rGO-**1**/GCE.

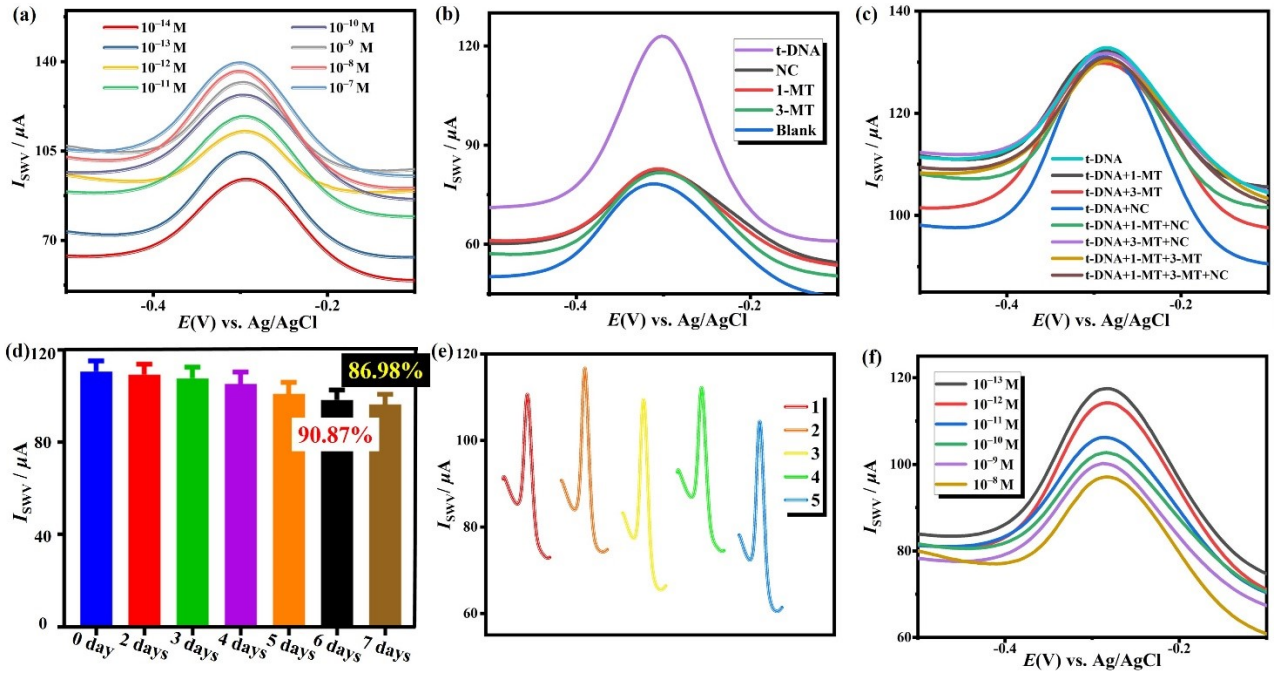

Fig. S22 (a) SWV curves of MB/dsDNA/Au-rGO-**1**/GCEs constructed by using different concentrations of t-DNA (10^{-14} / 10^{-13} / 10^{-12} / 10^{-11} / 10^{-10} / 10^{-9} / 10^{-8} / 10^{-7} M). (b) SWV curves of the specificity of MB/dsDNA/Au-rGO-**1**/GCE EDB for different DNA sequences. (c) SWV curves of the anti-interference capability of MB/dsDNA/Au-rGO-**1**/GCE EDB different interference DNA sequences. (d) The time-dependent stability of MB/dsDNA/Au-rGO-**1**/GCE EDB for t-DNA detection after stored for 2, 3, 4, 5, 6 and 7 days. (e) The repeatability of five MB/dsDNA/Au-rGO-**1**/GCE EDBs. (f) SWV curves of MB/dsDNA/Au-rGO-**1**/GCEs constructed by using different concentrations of t-DNA (10^{-13} / 10^{-12} / 10^{-11} / 10^{-10} / 10^{-9} / 10^{-8} M) in human serum solution diluted 1000 times by using the Tris–HCl solution.

Table S1 Brief summary of experimental conditions of OLLFATs.

OLLFATs	Raw materials	pH	Reaction medium	Temperature (°C)	Ref
$[Sb_7W_{36}O_{133}Ln_3M_2(CH_3COO)(H_2O)_8]^{17-}$ (Ln = La^{3+}–Gd^{3+}, M = Co^{2+}; Ln = Ce^{3+}, M = Ni^{2+}, Zn^{2+})	{SbW_9}, $MCl_2·6H_2O$ (Co or Ni) / $Zn(NO_3)_2·6H_2O$ $Ln(NO_3)_3·6H_2O$	4.60	CH_3COOH–CH_3COONa (1.0 M)	90	12
$[Ln_3Ni_9(OH)_9(SbW_9O_{33})_2(PW_9O_{34})_3(CH_3COO)_3]^{30-}$ (Ln = Dy^{3+}, Er^{3+})	{SbW_9}, $NiCl_2·6H_2O$, $Ln(NO_3)_3·6H_2O$, KH_2PO_4	5.50	CH_3COOH–CH_3COONa (1.0 M)	80	13
$[Dy_3(CH_3COO)_3(HPO_3)(WO_4)][B\text{-}\alpha\text{-}SbW_9O_{33}]_3^{25-}$ (Ln = Eu^{3+}, Dy^{3+}, Ho^{3+}, Er^{3+})	{SbW_9}, $Na_2WO_4·2H_2O$, KCl, H_3PO_3, $Ln(NO_3)_3·6H_2O$	5.50	CH_3COOH–CH_3COONa (2.0 M)	90	14
$[Ln(H_2O)_8]_2[Fe_4(H_2O)_8(thr)_2][B\text{-}\beta\text{-}SbW_9O_{33}]_2$ (Ln = Pr^{3+}, Nd^{3+}, Sm^{3+}, Eu^{3+}, Gd^{3+}, Dy^{3+}, Lu^{3+})	{SbW_9}, $FeCl_3·6H_2O$, $PrCl_3$, L-threonine	1.09–1.20	water	80	15
$[Ce_4(HP)W_8(H_2O)_{12}(H_2ptca)_2O_{28}][SbW_9O_{33}]_2^{12-}$ (Ln = La^{3+}, Ce^{3+}, Pr^{3+})	{SbW_9}, itaconic acid, $Ln(CH_3COO)_3$, H_3PO_3,	3.80–4.20	water	90	16
$[Ln_4(H_2O)_{14}W_7O_{15}(H_2MA)_4][SbW_9O_{33}]_2[HPSbW_{15}O_{54}]_2^{20-}$ (Ln = Nd^3, Pr^{3+})	{SbW_9}, $Na_2WO_4·2H_2O$, DL-malic acid, $Ln(CH_3COO)_3$, H_3PO_3	3.00	water	90	17
$[Ln_2(H_2O)_4\{WO_2(pic)\}_2(SbW_8O_{30})_2]^{10-}$ (Ln = La^{3+}, Pr^{3+})	{SbW_9}, $Ln(NO_3)_3·6H_2O$, 2-picolinic acid, LiCl	5.00	water	90	18
$[\{Ln(H_2O)\}\{Ln(pic)\}(Sb_3O_4)(SbW_8O_{31})(SbW_{10}O_{35})]_2^{24-}$ (Ln = Tb^{3+}, Dy^{3+}, Ho^{3+})	{SbW_9}, $Ln(NO_3)_3·6H_2O$, 2-picolinic acid, LiCl, Sb_2O_3	6.50	water	90	18
$[Ce(H_2O)_5(2,6\text{-}pdca)]_4H_2[Fe_4(H_2O)_6(SbW_9O_{33})_2]$	{SbW_9}, $Ce(NO_3)_3·6H_2O$ 2,6-pyridine dicarboxylic acid, $FeCl_3·6H_2O$	2.20	water	80	19
$[(Ln(H_2O)(OH)_2(CH_3COO))_3(WO_4)(SbW_9O_{33})_3]^{21-}$ (Ln = Tb^{3+},Dy^{3+}, Ho^{3+}, Er^{3+}, Y^{3+})	{SbW_9}, $Ln(NO_3)_3·6H_2O$	5.50	CH_3COOH–CH_3COONa (2.0 M)	80	22
$[H_2N(CH_3)_2]_9Na_{12}H_6\{[Ce_3(H_2O)_2W_8(Hgps)_2O_{20}][B\text{-}\alpha\text{-}SbW_9O_{33}]_4\}·66H_2O$	$SbCl_3$, $Na_2WO_4·2H_2O$, $Ce(NO_3)_3·6H_2O$, glyphosine	4.80–5.20	CH_3COOH–CH_3COONa (1.5 M)	90	This work

Table S2 Experimental explorations on the synthesis of 1.

	$SbCl_3$ (1.00 mM)	$Na_2WO_4 \cdot 2H_2O$	H_5gps	$Ce(NO_3)_3 \cdot 6H_2O$	$CH_3COOH-CH_3COONa$	pH	Growth time	Result (yield)
The effect of $CH_3COOH-CH_3COONa$ buffer concentration	1.0 mL	5.0 g	0.2 g	0.2 g	0–1.0 M, 15mL	5.00	> 20 days	**1** (13.53–15.48%)
					1.5–2.0 M, 15mL		1–2 days	**1** (27.83–30.48%)
The effect of $Ce(NO_3)_3 \cdot 6H_2O$ amount	1.0 mL	5.0 g	0.2 g	0.1 g	1.5 M, 15 mL	5.00	1–2 days	**1** (28.40–33.95%)
				0.2 g				
				0.4 g			—	precipitate
				> 0.4 g				
The effect of H_5gps amount	1.0 mL	5.0 g	0.1 g	0.2 g	1.5 M, 15 mL	5.00	1–2 days	**1** (24.93–32.53%)
			0.2 g					
			0.4 g				—	precipitate
			> 0.4 g					
The effect of pH variation	1.0 mL	5.0 g	0.2g	0.2 g	1.5 M, 15 mL	4.00	—	precipitate
						4.20		
						4.40	> 10 days	**1** (14.96–17.28%) and precipitate
						4.60		
						4.80	1–2 days	**1** (26.16–31.48%)
						5.00		
						5.20		
						5.40	> 10 days	**1** (13.25–15.48%) and precipitate
						5.50	—	precipitate

Table S3 Crystallographic data and structure refinements for 1.

	1
Empirical formula	$C_{26}H_{228}Ce_3N_{11}Na_{12}O_{236}P_4Sb_4W_{44}$
Formula weight	13868.71
Crystal system	Monoclinic
Space group	*Cc*
a, Å	37.8115(8)
b, Å	16.9387(4)
c, Å	41.2813(10)
α, deg	90
β, deg	106.1290(10)
γ, deg	90
V, Å^{-3}	25399.0(10)
Z	4
μ, mm^{-1}	20.938
F(000)	24700
D_c, g cm^{-3}	3.627
T, K	150(2)
Limiting indices	-45 ≤ *h* ≤ 44 -17 ≤ *k* ≤20 -45 ≤ *l* ≤ 49
Reflections collected/unique	77019 / 36282
R_{int}	0.0332
Data/restrains/parameters	36282 / 449 / 2700
GOF on F^2	1.064
R_1, wR_2 ($I > 2\sigma(I)$)[a]	0.0390, 0.1053
R_1, wR_2 (all data)	0.0401, 0.1059

Table S4 Comparison of the sensitivity of different EDBs for DNA sequence detection.

Detection platform	Detection method	Concentration range (M)	LOD	Ref.
3D G-Au NP/GCE	DPV	$1.0 \times 10^{-14} – 1.0 \times 10^{-7}$	9.41×10^{-15}	23
G/Au NR/PT/GCE	DPV	$1.0 \times 10^{-13} – 1.0 \times 10^{-10}$	4.03×10^{-14}	24
Au NPs/TB–GO/GCE	DPV	$1.0 \times 10^{-11} – 1.0 \times 10^{-9}$	2.90×10^{-13}	25
Graphene/GCE	DPV	$2.0\times 10^{-14} – 2.0 \times 10^{-9}$	8.20×10^{-15}	26
Au-rGO-**1**/GCE	SWV	$1.0 \times 10^{-14} – 1.0 \times 10^{-7}$	3.09×10^{-15}	This work

The limit of detection (LOD) is calculated according to $I_{SWV} + 3\sigma = I = k \lg C_{t\text{-}DNA} + b$ (I_{SWV} is the baseline value calculated as the average of the sensing signal without t-DNA from five experiments, and σ is the standard deviation of five I_{SWV}, k is the slope of the calibration equation, b is the intercept of the fitting equation, $C_{t\text{-}DNA}$ is the LOD for t-DNA detection).

References

1 G. M. Sheldrick, *SHELXL 97, Program for Crystal Structure Refinement*; University of Göttingen: Göttingen, Germany, 1997.

2 G. M. Sheldrick, *SHELXS 97, Program for Crystal Structure Solution*; University of Göttingen: Göttingen, Germany, 1997.

3 C. Pichon, A. Dolbecq, P. Mialane, J. Marrot, E. Rivière and F. Sécheresse, Square versus tetrahedral iron clusters with polyoxometalate ligands, *Dalton Trans.*, 2008, **1**, 71–76.

4 C. Pichon, A. Dolbecq, P. Mialane, J. Marrot, E. Rivière, M. Goral, M. Zynek, T. McCormac, S. A. Borshch, E. Zueva and F. Sécheresse, Fe_2 and Fe_4 clusters encapsulated in vacant polyoxotungstates: Hydrothermal synthesis, magnetic and electrochemical properties, and DFT calculations, *Chem. Eur. J.*, 2008, **14**, 3189–3199.

5 L. L. Liu, J. Jiang, G. P. Liu, X. D. Jia, J. W. Zhao, L. J. Chen and P. Yang, Hexameric to trimeric lanthanide-Included selenotungstates and their 2D honeycomb organic–inorganic hybrid films used for detecting ochratoxin A, *ACS Appl. Mater. Interfaces,* 2021, **13**, 35997–36010.

6 T. Yamase, H. Naruke and Y. Sasaki, Crystallographic characterization of the polyoxotungstate $[Eu_3(H_2O)_3(SbW_9O_{33})(W_5O_{18})_3]^{18-}$ and energy transfer in its crystalline lattices, *Dalton Trans.*, 1990, **5**, 1687–1696.

7 M. Bösing, I. Loose, H. Pohlmann and B. Krebs, New strategies for the generation of large heteropolymetalate clusters: The *β*-B-SbW_9 fragment as a multifunctional unit, *Chem. Eur. J.*, 1997, **3**, 1232–1237.

8 G. L. Xue, J. Vaissermann and P. Gouzerh, Cerium(III) complexes with lacunary polyoxotungstates. Synthesis and structural characterization of a novel heteropolyoxotungstate based on *α*-$[SbW_9O_{33}]^{9-}$ units, *Journal of Cluster Science*, 2002, **13**, 409–421.

9 X. Xu, Y. H. Chen, Y. Zhang, Y. F. Liu, L. J. Chen and J. W. Zhao, Rare-earth and antimony-oxo clusters simultaneously connecting antimonotungstates comprising divacant and tetravacant Keggin fragments, *Inorg. Chem.*, 2019, **58**, 11636–11648.

10 H.-P. Xiao, R.-T. Zhang, Z. Li, Y.-F. Xie, M. Wang, Y.-D. Ye, C. Sun, Y.-Q. Sun, X.-X. Li and S.-T. Zheng, Organoamine-directed assembly of 5p–4f heterometallic cluster substituted polyoxometalates: Luminescence and proton conduction properties, *Inorg. Chem.*, 2021, **60**, 13718–13726.

11 H.-P. Xiao, Y.-S. Hao, X.-X. Li, P. Xu, M.-D. Huang and S.-T. Zheng, A water-soluble antimony-rich polyoxometalate with broad-spectrum antitumor activities, *Angew. Chem. Int. Ed.*, 2022, **61**, e202210019.

12 B. Artetxe, S. Reinoso, L. S. Felices, L. Lezama, J. M. Gutiérrez-Zorrilla, C. Vicent, F. Haso and T. B. Liu, New perspectives for old clusters: Anderson–Evans anions as building blocks of large polyoxometalate frameworks in a series of heterometallic 3d–4f species, *Chem. Eur. J.*, 2016, **22**, 4616–4625.

13 J. Cai, X.-Y. Zheng, J. Xie, Z.-H. Yan, X.-J. Kong, Y.-P. Ren, L.-S. Long and L.-S. Zheng, Anion-dependent assembly of heterometallic 3d–4f clusters based on a lacunary polyoxometalate, *Inorg. Chem.*, 2017, **56**, 8439–8445.

14 X. Xu, X. Y. Liu, D. Wang, X. J. Liu, L. J. Chen and J. W. Zhao, $\{HPO_3\}$ and $\{WO_4\}$ simultaneously induce the assembly of tri-Ln(III)-incorporated antimonotungstates and their photoluminescence behaviors, *Inorg. Chem.*, 2021, **60**, 1037–1044.

15 J.-W. Zhao, J. Cao, Y.-Z. Li, J. Zhang and L.-J. Chen, First tungstoantimonate-based transition-metal–lanthanide heterometallic hybrids functionalized by amino acid ligands, *Cryst. Growth Des.*, 2014, **14**, 6217–6229.

16 S. S. Xie, J. Jiang, D. Wang, Z. G. Tang, R. F. Mi, L. J. Chen and J.W. Zhao, Tricarboxylic-ligand-decorated lanthanoid-inserted heteropolyoxometalates built by mixed-heteroatom-directing polyoxotungstate units: Syntheses, structures, and electrochemical sensing for 17*β*-estradiol, *Inorg. Chem.*, 2021, **60**, 7536–7544.

17 S. S. Xie, D. Wang, Z. X. Wang, J. C. Liu, L. J. Chen and J. W. Zhao, Dual-heteroatom-templated lanthanoid-inserted heteropolyoxotungstates simultaneously comprising Dawson and Keggin subunits and their composite film applied for electrochemical immunosensing of auximone, *Inorg. Chem. Front.*, 2022, **9**, 350–362.

18 L.-L. Li, H.-Y. Han, Y.-H. Wang, H.-Q. Tan, H.-Y. Zang and Y.-G. Li, Construction of polyoxometalates from dynamic lacunary polyoxotungstate building blocks and lanthanide linkers, *Dalton Trans.*, 2015, **44**, 11429–11436.

19 B. X. Zeng, Y. Zhang, Y. H. Chen, G. P. Liu, Y. Z. Li, L. J. Chen and J. W. Zhao, 3-D antimonotungstate framework based on 2,6-H_2pdca-connecting iron−cerium heterometallic Krebs-type polyoxotungstates for detecting small biomolecules, *Inorg. Chem.*, 2021, **60**, 2663–2671.

20 J. W. Zhao, C. M. Wang, J. Zhang, S. T. Zheng and G. Y. Yang, Combination of lacunary polyoxometalates and high-nuclear transition metal clusters under hydrothermal conditions: IX. A series of novel polyoxotungstates sandwiched by octa-copper clusters, *Chem. Eur. J.*, 2008, **14**, 9223–9239.

21 R. Chris, B. Valérie, G. M. Evan, R. Christian and B. Colette, Sensitization of lanthanoid luminescence by organic and inorganic ligands in lanthanoid-organic-polyoxometalates, *Inorg. Chem.*, 2012, **51**, 1142–1151.

22 E. Tanuhadi, E. Al-Sayed, G. Novitchi, A. Roller, G. Giester and A. Rompel, Cation-directed synthetic strategy using 4f tungstoantimonates as nonlacunary precursors for the generation of 3d−4f clusters, *Inorg. Chem.*, 2020, **59**, 8461–8467.

23 S. Q. Chen, Y. F. Cheng and G. Voordouw, Three-dimensional graphene nanosheet doped with gold nanoparticles as electrochemical DNA biosensor for bacterial detection, *Sens. Actuators*, *B*, 2018, **262**, 860–868.

24 H. Y. Huang, W. Q. Bai, C. X. Dong, R. Guo and Z. H. Liu, An ultrasensitive electrochemical DNA biosensor based on graphene/Au nanorod/polythionine for human papillomavirus DNA detection, *Biosens. Bioelectron.*, 2015, **68**, 442–446.

25 H.-P. Peng, Y. Hu, P. Liu, Y.-N. Deng, P. Wang, W. Chen, A.-L. Liu, Y.-Z. Chen and X.-H. Lin, Label-free electrochemical DNA biosensor for rapid detection of mutidrug resistance gene based on Au nanoparticles/toluidine blue–graphene oxide nanocomposites, *Sens. Actuators, B*, 2015, **207**, 269–276.

26 Z. J. Yin, H. F. Cui, Q. X. Shu, C. Jin, Y. Lin, J. Su, H. L. Huang, F. S. Liao, G. Q. Ma, N. Hong, Y. F. Jiang and H. Fan, Multi-signal amplification electrochemical DNA biosensor based on exonuclease III and tetraferrocene, *J. Mater. Chem. B*, 2020, **8**, 4143–4150.